JGP Journal of General Physiology

RESEARCH ARTICLE

The syndromic deafness mutation G12R impairs fast and slow gating in Cx26 hemichannels

Isaac E. García[1,2], Felipe Villanelo[1,3], Gustavo F. Contreras[1], Amaury Pupo[1], Bernardo I. Pinto[1], Jorge E. Contreras[4], Tomás Pérez-Acle[1,3], Osvaldo Alvarez[1,5], Ramon Latorre[1], Agustín D. Martínez[1], and Carlos González[1]

Mutations in connexin 26 (Cx26) hemichannels can lead to syndromic deafness that affects the cochlea and skin. These mutations lead to gain-of-function hemichannel phenotypes by unknown molecular mechanisms. In this study, we investigate the biophysical properties of the syndromic mutant Cx26G12R (G12R). Unlike wild-type Cx26, G12R macroscopic hemichannel currents do not saturate upon depolarization, and deactivation is faster during hyperpolarization, suggesting that these channels have impaired fast and slow gating. Single G12R hemichannels show a large increase in open probability, and transitions to the subconductance state are rare and short-lived, demonstrating an inoperative fast gating mechanism. Molecular dynamics simulations indicate that G12R causes a displacement of the N terminus toward the cytoplasm, favoring an interaction between R12 in the N terminus and R99 in the intracellular loop. Disruption of this interaction recovers the fast and slow voltage-dependent gating mechanisms. These results suggest that the mechanisms of fast and slow gating in connexin hemichannels are coupled and provide a molecular mechanism for the gain-of-function phenotype displayed by the syndromic G12R mutation.

Introduction

A family of proteins called connexins forms vertebrate gap junction channels and hemichannels. They are encoded by a multigene family that contains 21 members in humans (Söhl and Willecke, 2003). Connexins have four transmembrane segments (TM1–4) connected by two extracellular loops (EL1–2) and one intracellular loop, with cytosolic N- and C-terminal segments. Hemichannels are formed by oligomerization of six connexin monomers and communicate between the cytoplasm and the extracellular milieu. At plasma membrane appositional zones, hemichannels can dock to compatible hemichannels in the adjacent cell to form gap junction channels, providing a direct pathway for intercellular communication (Goodenough et al., 1996; Gaietta et al., 2002; Segretain and Falk, 2004). Connexin hemichannels are regulated by pH (Bevans and Harris, 1999), phosphorylation (Lampe and Lau, 2000), and divalent cations (Verselis et al., 1994; Verselis and Srinivas, 2008) and exhibit two voltage-dependent gating mechanisms: loop (slow) gating, which closes hemichannels at hyperpolarizing voltages, and Vj (fast) gating, which drives hemichannels into a subconductance state at depolarizing voltages (Trexler et al., 1996; Bargiello et al., 2012; Oh and Bargiello, 2015).

Mutations in the Cx26 gene are the main cause of genetic deafness (Bergoffen et al., 1993; Kelsell et al., 1997, 2000; Arita et al., 2006; Arora et al., 2008; Dobrowolski and Willecke, 2009), with a prevalence of ∼50% of cases worldwide (Kelsell et al., 1997). Some mutations in Cx26 produce syndromic deafness in which severe deafness is accompanied by extensive damage in other tissues, such as in keratitis ichthyosis deafness (KID) syndrome, in which patients also present skin abnormalities (such as palmoplantar keratoderma and erythrokeratoderma) and strong inflammation of the cornea (Yotsumoto et al., 2003; van Steensel et al., 2004; Arita et al., 2006; Mazereeuw-Hautier et al., 2007). To date, there is agreement that nonsyndromic deafness-associated Cx26 mutations reduce gap junction channel function, the degree of which correlates well with deafness severity. In contrast, Cx26 mutations associated with syndromic deafness produce hyperactive or leaky hemichannels in their homomeric (Gerido et al., 2007; Lee et al., 2009; Sánchez et al., 2010, 2013, 2016) and heteromeric (García et al., 2015) configurations. KID-associated mutations cluster at the N terminus and the TM1/EL1 segment of Cx26 in amino acid residues that face the channel pore (García et al., 2016). These regions are critical for regulation of gating.

[1]Centro Interdisciplinario de Neurociencia de Valparaíso, Facultad de Ciencias, Universidad de Valparaíso, Valparaíso, Chile; [2]Laboratory of Molecular Physiology and Biophysics, Facultad de Odontología, Universidad de Valparaíso, Valparaíso, Chile; [3]Computational Biology Laboratory, Fundación Ciencia & Vida, Santiago, Chile; [4]Department of Pharmacology, Physiology, and Neuroscience, New Jersey Medical School, Rutgers University, Newark, NJ; [5]Departamento de Biología, Facultad de Ciencias, Universidad de Chile, Santiago, Chile.

Correspondence to Carlos González: carlos.gonzalezl@uv.cl; Agustín D. Martínez: agustin.martinez@uv.cl; Ramon Latorre: ramon.latorre@uv.cl.

Previous studies have shown that KID-causing mutations in the TM1/EL1 segment affect hemichannel voltage dependence and permeability and impair regulation by extracellular Ca^{2+} ($[Ca^{2+}]_o$; Gerido et al., 2007; Lee et al., 2009; Sánchez et al., 2010, 2013, 2016). It has recently been reported that the N-terminal mutation N14K selectively disrupts channel slow gating without apparent changes in its fast gating (Sánchez et al., 2016). The finding that N14K mutation does not affect the fast gating mechanism is intriguing because amino acids in the N terminus have been previously implicated in this gate (Trexler et al., 1996; Maeda et al., 2009; Bargiello et al., 2012).

Among the syndromic deafness-associated mutations located in the Cx26 N terminus, G12R is a good candidate to investigate the mechanisms underlying the observed gain of hemichannel function. Indeed, glycine at position 12 is conserved among β connexins, and mutations at this position have been found in patients suffering from erythrokeratodermia variabilis (Cx30.3 *GJB4*; Cx31 *GJB3*; Richard et al., 1998) and Charcot-Marie-Tooth disease (Cx32 *GJB1*; Bergoffen et al., 1993).

Here, we studied the biophysical properties of the G12R mutant expressed in *Xenopus laevis* oocytes and the structural changes induced by the mutation by molecular dynamics simulations, thus providing insight into the molecular mechanisms underlying the gain of hemichannel function of G12R. Remarkably, we found that the G12R mutation strongly impairs the fast gate and modifies the slow gate kinetics of hemichannels. At the single-hemichannel level, this mutation greatly decreases the probability of finding the hemichannel in the subconductance state that is characteristic of the fast gate activation. We propose that at the molecular level, the mutation allows an interaction between R12 and R99, fixing the N terminus in a new position toward the cytoplasm, thereby preventing its action as a blocking gating particle. Finally, these results favor the idea that the fast and slow gates are functionally coupled. Knowledge of the structural and functional bases for the gain of hemichannel function of Cx26 syndromic mutants can lead to development of novel therapeutic strategies.

Materials and methods

Site-directed mutagenesis and channel expression

The cDNA for hCx26 (OriGene) was subcloned in the pGEM-HA vector (Promega) for expression in *X. laevis* oocytes. Mutations of hCx26 were produced with Quick-Change II Site-Directed Mutagenesis kits (Agilent Technologies). Site-directed mutagenesis was confirmed by sequencing at Macrogen. Nhe1-linearized hCx26 WT and mutant DNAs were transcribed in vitro to cRNAs using the T7 Ultra mMessage mMachine kit (Ambion). RNA integrity was confirmed by running the samples on an agarose gel. The RNA concentration was determined using UV spectrophotometer (UV-1700; Pharma Spec). RNA stock was diluted in RNA-free water to a final concentration of 1 µg/µl and stored at −80°C. The follicular membrane of the oocytes was removed by digestive treatment with collagenase type II (Worthington Biochemical Corp.). To efficiently reduce endogenous Cx38 expression, an antisense oligonucleotide against Cx38 (1 µg/µl; 5′-GCTTTAGTAATT CCCATCCTGCCATGTTTC-3′; Integrated DNA Technologies) was injected 4 h after harvesting the oocytes (Ebihara, 1996). Defolliculated oocytes were injected with 41 nl of the desired cRNA using a Drummond Scientific Nanoinjector and maintained at 18°C in ND96 medium (in mM): 96 NaCl, 2 KCl, 1.8 $CaCl_2$, 1 $MgCl_2$, and 5 HEPES, pH 7.5, adjusted with NaOH. Macroscopic currents were evaluated 24 or 48 h after cRNA injection in oocytes bathed in an extracellular solution containing 1.8 mM Ca^{2+}. Oocytes were injected with 30 nl BAPTA (1,2-bis(*o*-aminophenoxy)ethane-*N*,*N*,*N*′,*N*-tetraacetic acid) at 5 µM to overcome the endogenous activation of Ca^{2+}-activated chloride channels. Oocytes were maintained in ND-96 for 30 min for recovery. All experiments were performed at room temperature (20–22°C).

Electrophysiology

Macroscopic Cx26 hemichannel currents expressed in *X. laevis* oocytes were recorded using the two-electrode voltage-clamp technique with an oocyte clamp (OC-725C; Warner Instruments). Micropipettes housing the two Ag/AgCl electrodes to measure intracellular potential (voltage electrode) and inject currents (current electrode) into the oocyte were pulled to a resistance of 0.5–1.5 MΩ and filled with 3 M KCl. The bath solutions contained (in mM) 118 NaCl, 2 KCl, and 5 HEPES, pH 7.4, with variable Ca^{2+} concentration from 0.01 to 10 mM. The bath was connected to two 3-M KCl pools using agar salt bridges. The Ca^{2+} concentrations in the bath were changed using a custom-made perfusion system. Currents were recorded 1–3 d after cRNA injection. Currents were low-pass filtered at 200 Hz and sampled and digitized at 1 kHz. Membrane currents were recorded from oocytes under two-electrode voltage clamp in response to depolarizing voltage steps from a holding potential of −80 mV, stepped in 10- or 20-mV increments from −60 mV to 50 or 60 mV, and returned to −80 mV.

Single-hemichannel recording was done using cell-attached and inside-out patch clamp. Removal of the oocyte vitelline membrane of selected oocytes was performed manually using forceps (Word Precision Instruments). Oocytes were placed in a recording chamber containing the internal patch solution, which consisted of (in mM) 140 KCl, 1.8 $CaCl_2$, 1 $MgCl_2$, 5 HEPES, and 3 EGTA, pH adjusted to 8 with KOH. The bath solution was connected to the 3-M KCl ground solution pool via an agar bridge. Patch micropipettes were made of glass borosilicate capillaries (World Precision Instruments) pulled on a horizontal puller (Sutter Instrument Co.) and fire polished using a custom microforge to a resistance ranging between 500 kΩ and 1 MΩ when filled with internal patch solution. Patch clamp was performed using an Axopatch 200B amplifier (Axon Instruments; Molecular Devices). The voltage command and current output were filtered with eight-pole Bessel low-pass filters (Frequency Devices). The −3-decibel frequency was 200 Hz for the current input, which was digitized at 1 kHz using a 16-bit A/D converter data acquisition system (Digidata1322; Axon Instruments; Molecular Devices). Recordings were performed holding the voltage at the desire potentials using Clampex 8 acquisition software (Axon Instruments; Molecular Devices).

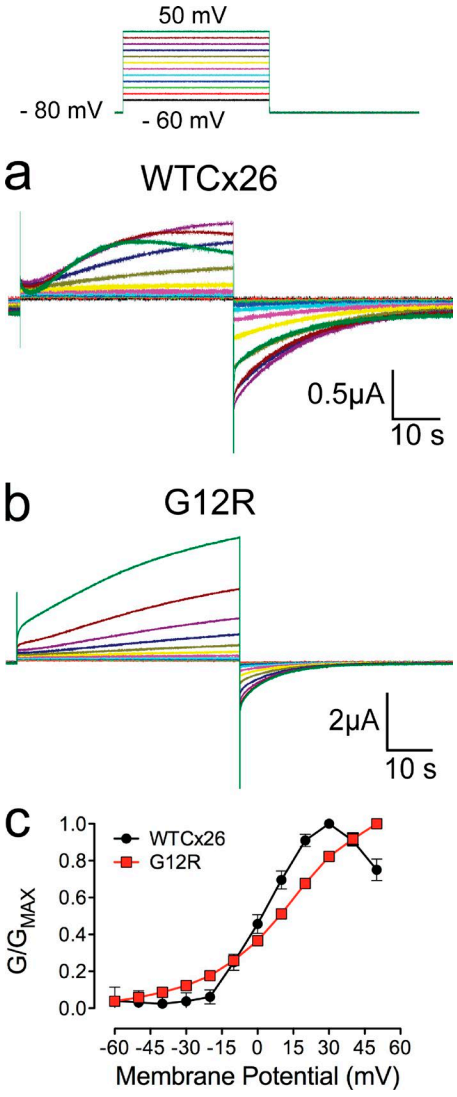

Figure 1. **WT and G12R Cx26 gating kinetics and voltage dependence.** Membrane currents were recorded from oocytes under two-electrode voltage clamp in response to depolarizing voltage steps from a holding potential of −80 mV, stepped in 10-mV increments from −60 to 50 mV, and returned to −80 mV. **(a and b)** Representative trace of macroscopic currents recorded in oocytes expressing WTCx26 (a) or G12R (b). **(c)** Normalized conductance–voltage relationship of WTCx26 and G12R hemichannels. Data obtained from the instantaneous tail currents taken at −80 mV and measured after 40-s test pulse for each voltage tested. Data symbols and error bars represent mean ± SEM; n = 20 oocytes from five different batches.

Measurement of Ca^{2+} dose–response curves

Calcium dose–response measurements were performed essentially as described previously (Lopez et al., 2013). Ca^{2+} dose–response experiments were performed in batches of oocytes showing low or no expression of endogenous currents when bathed in an extracellular solution containing Ca^{2+} concentrations ranging from 0.01 to 10 mM. Because of the slow kinetics of WTCx26 activation and deactivation, Ca^{2+} dose–response experiments were obtained by assessing the peak tail currents after reaching current saturation during a depolarizing pulse from −80 to 0 mV, at different $[Ca^{2+}]_o$ concentrations. To minimize the damage caused to the oocyte by the opening of hemichannels under these experimental conditions, no more than four different Ca^{2+} concentrations, including 0.01 mM Ca^{2+}, were tested to prevent damage to the oocytes and for the reproducibility of the currents measured in response to Ca^{2+} changes. Data were adjusted to a Hill equation of the following form:

$$I/I_{max} = \frac{1}{1 + ([Ca^{2+}]/K_d)^n}, \quad (1)$$

where the fractional current is I/I_{max}, I_{max} is the maximal tail current measured at 0.01 mM Ca^{2+}, I is the instantaneous tail current recorded at a particular Ca^{2+} concentration measured at −80 mV after a 40-s depolarization to 0 mV, K_d is an apparent Ca^{2+} dissociation constant (in mM), and n is the Hill coefficient.

Deactivation time constants from tail currents were determined by fitting instantaneous tail currents measured up to 10 s after reaching steady state to single exponential functions using Clampfit 10.4 software (Molecular Devices).

Molecular dynamics simulations

The WTCx26 hemichannel model was constructed using the coordinates of the crystallographic structure of the Cx26 gap junction channel (Maeda et al., 2009; Protein Data Bank accession no. 2ZW3). Coordinates of residues Met1, intracellular loop, C-terminal domain, and side chains for residues K15, S17, and S19 were lacking from the x-ray structure. All missing residues in the crystal structure of Cx26 were modeled using Modeler (Martí-Renom et al., 2000), keeping the original x-ray coordinates fixed and considering the hexameric symmetry of the hemichannel. The models were evaluated using a statistical potential algorithm derived exclusively from membrane proteins (Postic et al., 2015). Hydrogen atoms were assigned using the psfgen module of the Visual Molecular Dynamics software, and protonation states were assigned according to the pKa values predicted by PROPKA 3.0 (Olsson et al., 2011). Disulfide bonds identified in the crystal structure were created between C53–C180, C60–C174, and C64–C169 in each connexin subunit. The WTCx26 hemichannel was then inserted into a POPC (1-palmitoyl-2-oleoylsn-glycero-3-phosphocholine) lipid membrane. The protein domains were arranged with regard to the hydrocarbon core of the lipid bilayer using the Orientations of Proteins in Membranes database (Lomize et al., 2006). As previously described (Kwon et al., 2011), a 150 × 150 × 110–Å box including the protein, lipids, TIP3 water molecules, and 150 mM KCl was generated using the membrane builder module of CHARMM-GUI. The CHARMM-22 and CHARMM-36 force fields were used for protein and lipids, respectively. An initial system equilibration of 375 ps at 303 K was performed using the protocol developed by Woolf and Roux (1996). To obtain a relaxed system, initial force constraints were gradually reduced using constant number of particles, volumen, and temperature (NVT) dynamics. Then, the system was equilibrated for 100 ns at 310 K using constant number of particles, pressure, membrane surface tension, and temperature (NPnAT) dynamics with no constraints. Both methods were applied using the Langevin temperature control. From the final frame of equilibration, we started four independent molecular dynamics simulations of

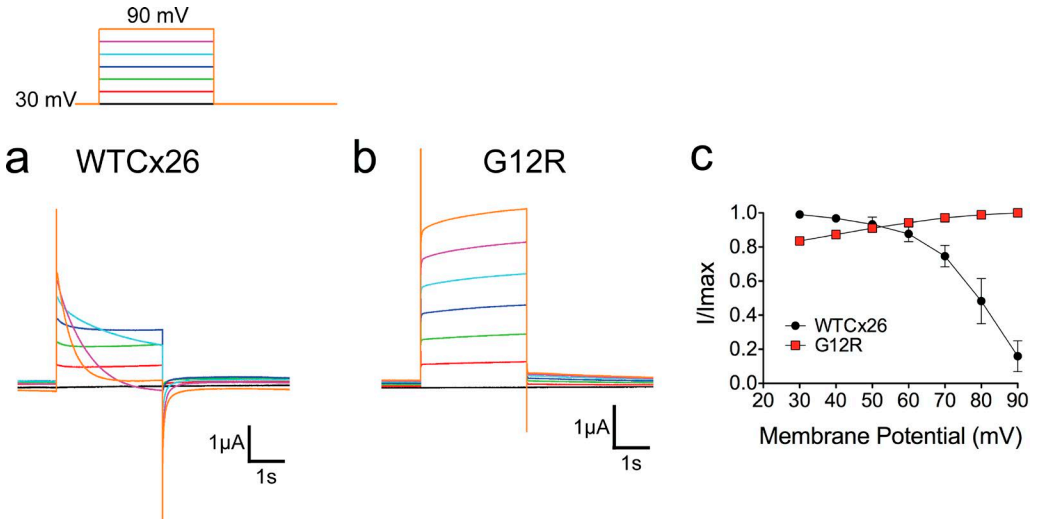

Figure 2. **G12R impairs fast gating.** Membrane currents were recorded from oocytes under two-electrode voltage clamp in response to depolarizing voltage steps from a holding potential of 30 mV, stepped in 10-mV increments to 90 mV, and returned to 30 mV. **(a and b)** Representative trace of macroscopic currents recorded in oocytes expressing WTCx26 (a) or G12R (b). **(c)** Current–voltage relationship of WTCx26 and G12R hemichannels. Data symbols and error bars represent mean ± SEM; *n* = 10 oocytes from three different batches.

20 ns. We started these simulations using different seeds and restarting the velocities from a Maxwell distribution. NPnAT dynamics were used for data collection and statistical analysis, with set points of 1 atm and 310 K using the Nose–Hoover method and Langevin dynamics for temperature and piston fluctuation control, with a damping coefficient of 1 ps. This simulation protocol was repeated three independent times starting from the crystal structure, giving $n = 12$ simulations for data analysis. All simulations were performed using NAMD 2.9. The particle mesh Ewald (PME) method was used for full long-range electrostatics within a relative tolerance of 10^{-6}. A cutoff distance of 12 Å was applied to real-space Ewald interactions, with a smooth switching function applied between 10 and 12 Å to account for Van der Waals interactions. The SHAKE algorithm was applied to constrain bond lengths to all hydrogen atoms.

The averages and distributions shown for the N terminus (Figs. 6, S1, S2, S3, and S4) were taken from the production simulations of 20 ns. The data for each monomer were calculated and compiled for histogram analysis, using the same amount of bins and the same limits. Curves were smoothed using the Lowess method.

Online supplemental material

Fig. S1 shows the geometrical distance of the N terminus of WTCx26 or G12R with reference to the center of mass of the protein. Fig. S2 shows the analysis of the local bending angles of TM2 near the proline kink in search for structural changes induced by G12R. Fig. S3 shows the root mean square deviation analysis derived from molecular dynamics simulations. Fig. S4 shows the correlation between the N-terminal displacement and side chain of R12 and also demonstrates no trapping in a local minimum in our simulations. Fig. S5 represents ensemble averages of single hemichannels for WTCx26, G12R, and G12/R99A and shows that single-hemichannel activity recapitulates the macroscopic current in all conditions.

Results

G12R mutant hemichannel shows a defective fast gate

To investigate whether the G12R mutation modifies the biophysical properties of Cx26 hemichannels, we expressed WTCx26 and the G12R mutant variant in *X. laevis* oocytes and performed electrophysiological recordings. Depolarization of oocytes expressing WTCx26 to 0 up to 60 mV from a holding potential of −80 mV induced a slowly activating current that reaches a maximum value of ∼30 mV and then decreases at higher voltages (Fig. 1, a and c). The decrease in the amplitude of the macroscopic current is the result of the activation of the fast gating mechanism (Trexler et al., 1996). When the same voltage protocol was applied to G12R-expressing oocytes, the induced macroscopic currents were larger than those produced by WTCx26 hemichannels, and the current amplitude increased with successive depolarizing voltage steps (Fig. 1, b and c).

To discard the possibility that large and prolonged depolarization was activating endogenous currents in oocytes that could mask the activation of the fast gate in G12R hemichannels, we performed a fast gating voltage protocol (Pinto et al., 2016). When depolarizing pulses were applied from a holding voltage of 30 mV, macroscopic WTCx26 hemichannel currents showed an initial rise followed by decay to a steady state, a clear demonstration that the fast gate is operative (Fig. 2, a and c). In contrast, G12R hemichannel currents increased with depolarizing voltages that in the WTCx26 hemichannels promote a clear macroscopic current decrease, suggesting that their fast gate is defective (Fig. 2, b and c). To confirm these observations, we performed single-hemichannel recordings from inside-out patches containing WTCx26 or G12R hemichannels (Fig. 3). Acquisition was performed using the fast gate voltage protocol. Ensemble averages from single hemichannels recordings in WTCx26 or G12R hemichannels mimic the kinetics of the currents observed at the macroscopic level. Accordingly, the analysis of the time constant deactivation kinetics in WTCx26 at macroscopic and

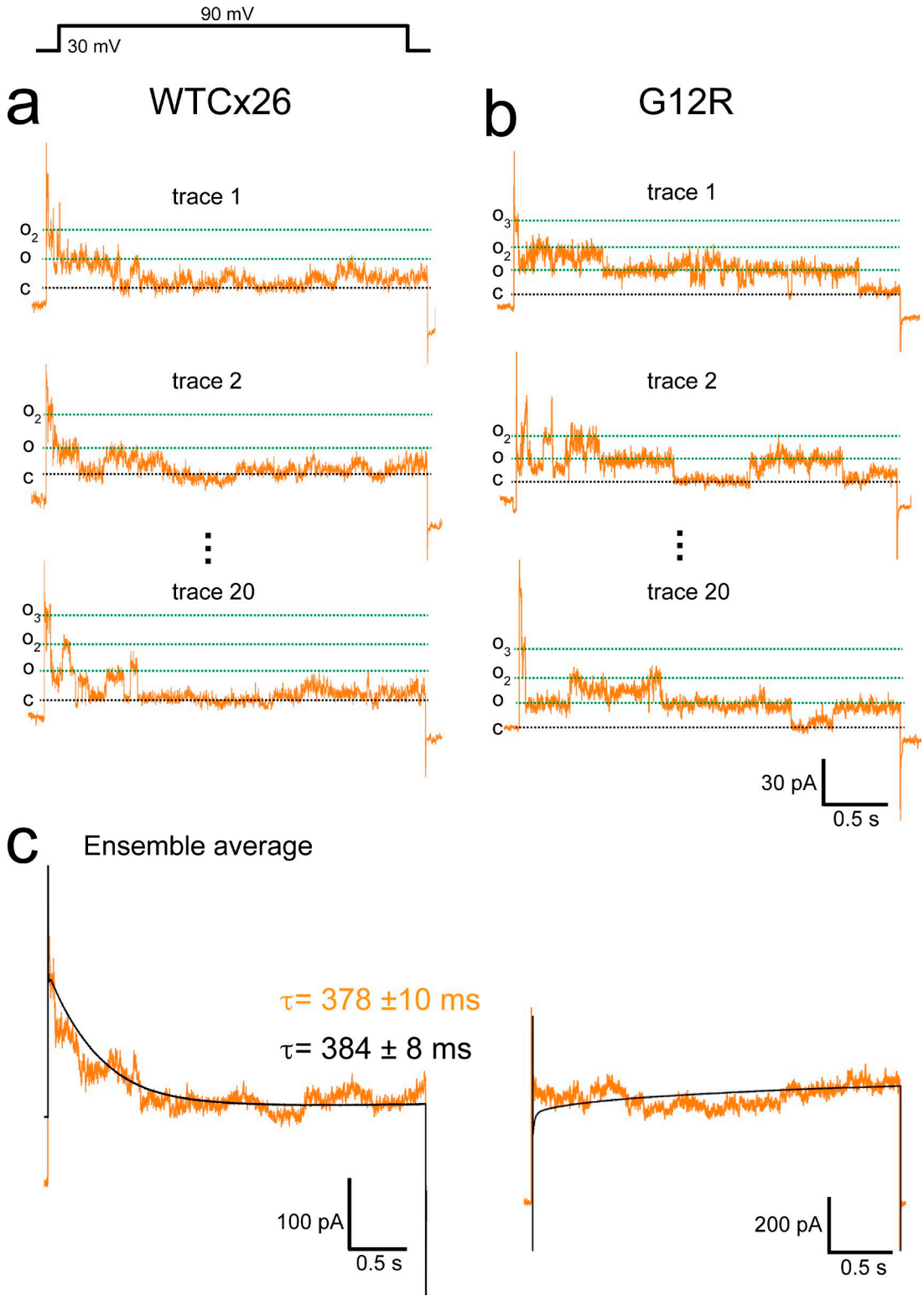

Figure 3. **Single-hemichannel activity recapitulates the macroscopic currents. (a and b)** Representative examples of patch-clamp recordings from excised inside-out patches containing WTCx26 (a) or G12R (b) hemichannels. Traces shown were obtained in response to a 3-s test pulse at 90 mV from and returning to a holding potential of 30 mV (mimicking the fast gate macroscopic protocol). Dashed lines represent the closed state (C) and the fully open state (O; subscript numbers indicate two or more channels opening). Each trial consisted of 20 sweeps that were ensemble averaged to recapitulate the kinetics of the macroscopic currents. **(c)** The ensemble average (orange trace) and the macroscopic trace (black trace) obtained at 90 mV were superimposed for comparison. The time constant of the deactivation kinetics from WTCx26 hemichannel was obtained by fitting the traces to a single exponential. No significant differences were observed. τ values represent mean ± SEM; *n* = 15 oocytes from three different batches.

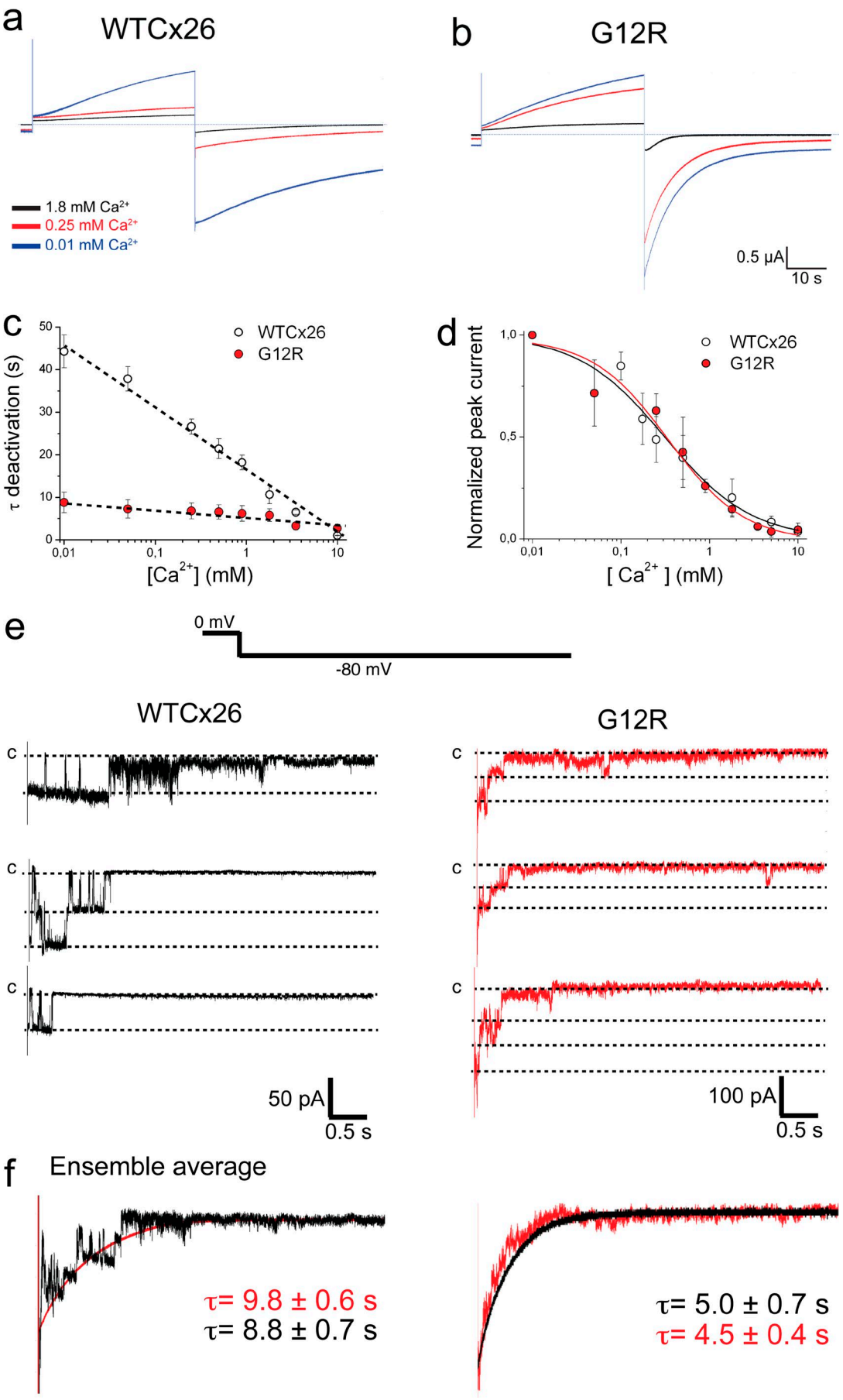
a
WTCx26
1.8 mM Ca2+
0.25 mM Ca2+
0.01 mM Ca2+
b
G12R
0.5 µA
10 s
c
τ deactivation (s)
WTCx26
G12R
[Ca2+] (mM)
d
Normalized peak current
WTCx26
G12R
[Ca2+] (mM)
e
0 mV
-80 mV
WTCx26
G12R
c
50 pA
0.5 s
100 pA
0.5 s
f
Ensemble average
τ= 9.8 ± 0.6 s
τ= 8.8 ± 0.7 s
τ= 5.0 ± 0.7 s
τ= 4.5 ± 0.4 s

single-hemichannel levels gave similar values (Fig. 3, a and b). Altogether, these results strongly indicate that the fast gate is defective in G12R hemichannels.

G12R hemichannels exhibited fast deactivation kinetics associated with an impaired slow gate

We observed differences in the kinetics of the deactivation between WTCx26 and G12R hemichannel currents (Fig. 1). Because channel closure at hyperpolarizing membrane potentials is regulated by the slow gating mechanism (Verselis et al., 2009), we determined the current deactivation time constants of WTCx26 and G12R hemichannels at different concentrations of $[Ca^{2+}]_o$. The deactivation time constant of WTCx26 hemichannels was ∼44 s at 0.01 mM $[Ca^{2+}]_o$ and decreased to 2 s at 10 mM $[Ca^{2+}]_o$ (Fig. 4, a and c), in agreement with the inverse linear relationship between the time constant of current decay and the logarithm of $[Ca^{2+}]_o$ reported previously for WTCx26 hemichannels (Lopez et al., 2013). In contrast, G12R hemichannels exhibited a deactivation time constant that was essentially independent of the $[Ca^{2+}]_o$; its value was 7 ± 0.5 s in 0.01 mM $[Ca^{2+}]_o$ and 5 ± 0.7 s in 1.8 mM $[Ca^{2+}]_o$ (Fig. 4, b and c). Ensemble averages from single hemichannels recordings in WTCx26 or G12R exposed to 1 mM Ca^{2+} mimic both the kinetics and deactivation time constants obtained from macroscopic hemichannel currents (Fig. 4, e and f), confirming that the slow gate is also impaired by the N terminus mutation G12R.

Because the Ca^{2+} sensitivity of the deactivation kinetics is altered in G12R hemichannels, we compared the apparent affinity constant (K_d) of WT and Cx26 mutant hemichannels for Ca^{2+}. The estimated K_d (mM) for Ca^{2+} was 0.31 ± 0.06, with a Hill coefficient (n) of 0.89 ± 0.12 for WTCx26 hemichannels (Fig. 4 d, open circles). Remarkably, the K_d for Ca^{2+} and n for G12R hemichannels were 0.34 ± 0.07 and 1.01 ± 0.15, similar to WTCx26 values (Fig. 4 d, red circles). These results are intriguing because the time constant of the deactivation is strongly Ca^{2+} dependent for WTCx26 hemichannels but not for G12R hemichannels, which suggests that either the kinetics of the voltage-dependent deactivation of G12R hemichannels is strongly accelerated in the absence of Ca^{2+} or that the current has not reached a steady state by the end of the depolarization pulse to 0 mV.

The transition to the subconductance state in the G12R mutant is greatly hindered

We have previously demonstrated that the relative rate of ethidium uptake is several-fold greater for G12R than for WTCx26 hemichannels (García et al., 2015). Thus, the increased macroscopic hemichannel activity induced by G12R could be explained by augmented single-hemichannel conductance and/or an increased hemichannel open probability. To distinguish between these, we used cell-attached or inside-out macropatches from *X. laevis* oocytes expressing either WTCx26 or G12R. At 20 mV, WTCx26 hemichannels (Fig. 5 a) exhibited a high open probability with few and brief transitions to a subconductance state (O*r*) occurring in WTCx26. In WTCx26 hemichannels, these transitions became more evident and longer when the patch membrane was depolarized to 40 mV, associated with reduction of the open probability of the fully open state (Fig. 5 a, trace at 40 mV). After the onset of the depolarizing step at 60 mV, single WTCx26 hemichannels enter a subconductance state, briefly visiting the open state afterward, then return to the subconductance state, and finally reach the closed state, dramatically reducing the open probability of the fully open state (Fig. 5 a, trace at 60 mV). In contrast, G12R hemichannel single-channel currents very seldom visit this subconductance state; instead, direct transitions between the fully open and closed states can be observed at any of the voltages tested, revealing defective fast gating activation in G12R hemichannels (Fig. 5 b). In contrast to WTCx26 hemichannels, both the open probability and mean open time of the fully open state increase with increasing voltages (Fig. 5 b). The single-channel behaviors of WTCx26 and G12R hemichannels are in agreement with the kinetics of the macroscopic currents (Figs. 2, a and b).

Linear regression analysis of the single hemichannel current versus voltage relationship revealed that the single-channel conductance of the fully open G12R hemichannels did not differ from that of WTCx26 (335 ± 9 vs. 334 ± 6 pS, respectively). These results demonstrate that the gain of function of the mutant hemichannel is caused by a marked increase in the single-hemichannel open probability.

Molecular modeling suggests that G12R displaces the N terminus toward the cytoplasm

To determine the molecular mechanisms underlying G12R hemichannel functioning, we performed molecular dynamics simulations. These simulations evince that the all-frame averages of the inner topology and radius of the pore along the z axis were similar between WTCx26 and G12R hemichannels (Fig. 6, a and b). The minimum pore diameter was ∼5.5 Å and 5.6 Å for WTCx26 and G12R, respectively, and occurred at the

Figure 4. **Fast deactivation kinetics in G12R hemichannels. (a and b)** A pulse from a holding potential of −80 to 0 mV and returned to −80 mV was applied to analyze tail currents and their deactivation kinetics in oocytes expressing WTCx26 (a) and G12R (b). Traces show the currents elicited in oocytes bathed in extracellular solution containing 1.8 mM Ca^{2+} (black traces), 0.25 mM Ca^{2+} (red traces), or 0.01 mM Ca^{2+} (blue traces). **(c)** Time constants of the deactivation as a function of Ca^{2+} concentration plotted using a semilogarithmic scale. The dotted lines represent the best linear fit to the WTCx26 and G12R mutant hemichannels' time-constant data. **(d)** Graph depicting normalized peak hemichannel tail currents as a function of Ca^{2+} concentration in WTCx26 (open circles) and G12R (red circles). Solid lines are the best fit to the data using a Hill equation for WTCx26 (black line) and G12R (red line; Eq. 1). The data points represent mean ± SEM; n = 10. **(e)** Representative examples of patch-clamp recordings from excised inside-out patches containing WTCx26 or G12R hemichannels. Traces shown were obtained in response to a 45-s test pulse at 0 mV from a holding potential of −80 mV and returned to −80 mV during an additional 45 s. Dashed lines represent the closed state (C) and the opening of hemichannels. Each trial consisted of 10 sweeps that were ensemble averaged to recapitulate the kinetics of the macroscopic currents. **(f)** The ensemble averages (black trace for WTCx26; red trace for G12R) and the macroscopic traces (red trace for WTCx26; black trace for G12R) obtained at −80 mV were superimposed for comparison. The time constant of the deactivation kinetics from WTCx26 and G12R hemichannels was obtained by fitting the traces to a single exponential. No significant differences were observed. τ values represent mean ± SEM; n = 15 oocytes from three different batches.

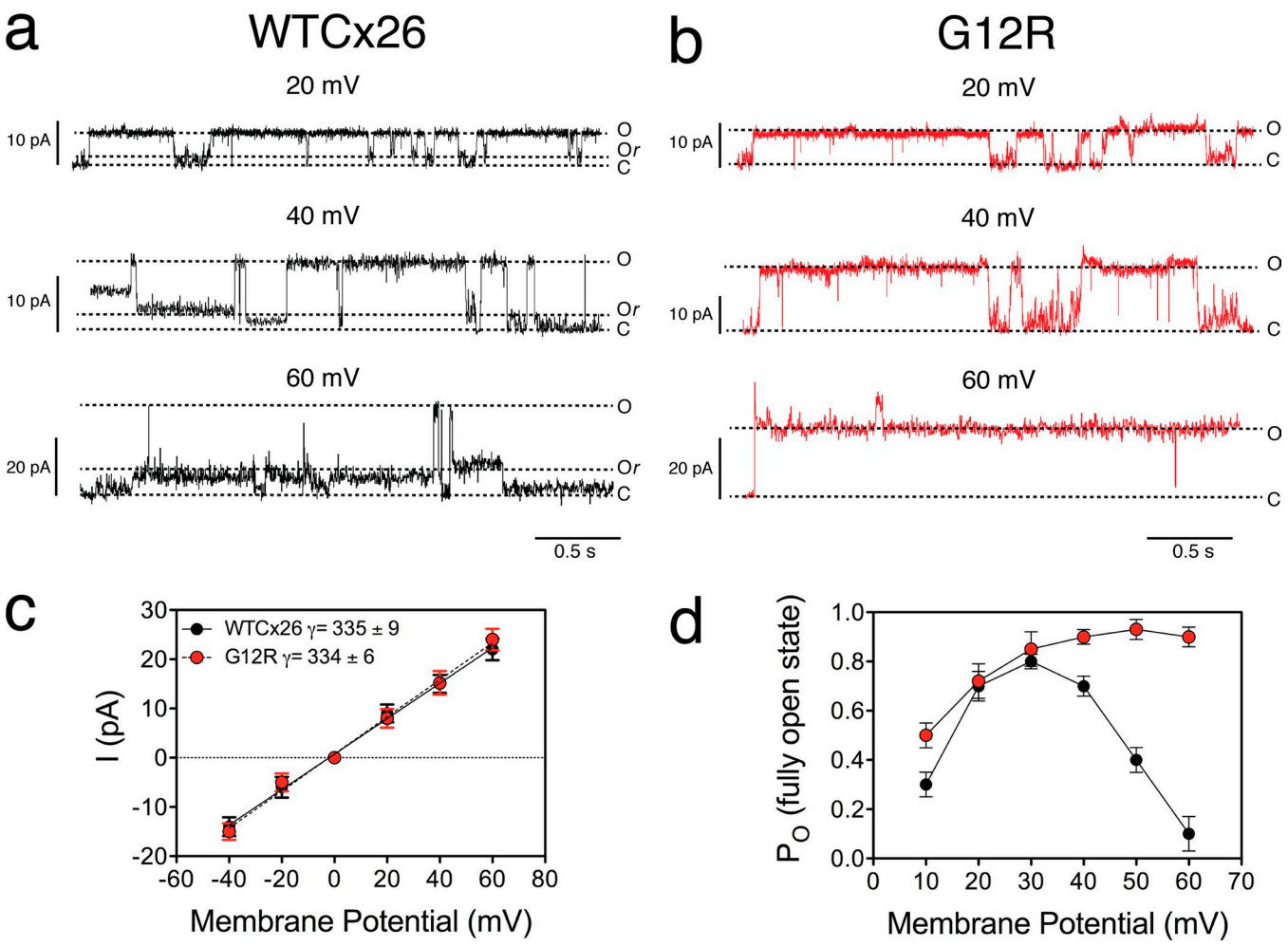

Figure 5. **The G12R mutation increases open probability without modifying single-channel conductance. (a and b)** Representative traces of WTCx26 (a) or G12R (b) single channels recorded at 20, 40, and 60 mV. The dashed lines represent the closed state (C), the fully open state (O), and the subconductance state (O*r*) of hemichannels. Note that conductance substates occur rarely and show fast kinetics in G12R hemichannels. **(c)** Graph depicting the plot of the current amplitude (I, pA) of the fully open state O obtained at different voltages (millivolts) for WTCx26 (black circles) and G12R (red circles). Black solid (WTCx26) and dashed (G12R) lines represent the best linear regression fit. The slope of the I-V relationship determined fully open state O slope conductance (measured at 0 mV). **(d)** Graph depicting the plot of the open probability (P_o) of the fully open state at different voltages (millivolts) for WTCx26 (black circles) and G12R (red circles). The data points represent mean ± SEM; *n* = 20 oocytes from five different batches.

level of the N terminus. However, this domain appears slightly displaced toward the cytoplasm in G12R hemichannels (Fig. 6 b, arrow between blue dashed lines). Correlation analysis between the N-terminal displacement and the side-chain angle of G12R in relation to the z axis shows no trapping on a local minimum during our simulations (Fig. S4).

To determine the basis for this displacement, we analyzed the position of the N terminus in WT and mutant Cx26 by measuring the geometrical distance between the centers of mass of the N terminus with respect to the center of mass of the whole structure. The distribution of distances in WTCx26 showed the main peak at 5.7 Å and a small peak at 7.5 Å (Fig. S1, black line). In contrast, G12R exhibits the main peak at 7.5 Å, a lower peak at 5.2 Å, and several low-frequency peak tails that can be observed up to 12 Å (Fig. S1, red line). This analysis confirms that the N terminus of G12R hemichannels is displaced toward the cytoplasm, in agreement with the pore radius profile analysis (Fig. 6 b). Moreover, the asymmetrical shape of the peak distribution in G12R indicates a more asymmetrical dynamic behavior of the monomers than in WTCx26. These results indicate that the N terminus of G12R hemichannels appears to be closer to the cytoplasm and is capable of acquiring a different molecular conformation than in the WT hemichannel.

We next explored which interactions in G12R might contribute to stabilizing the altered conformation of its N terminus. Because of physical proximity, the more likely interactions of the N terminus might take place with the intracellular loop. To explore this possibility, we sought to determine potential contacts between the mutated position 12 and an extended intracellular loop (from residue 90 to 140). We measured the distance between the guanidyl moiety and every residue in the extended intracelluar loop. The arginine 12 from five of the six protomers in a G12R hemichannel exhibited proximity with several residues in the intracellular loop (Table 1). These residues were A92, M93, V95, Y97, R99, and H100, with R99 being the most frequent (Fig. 6 c). These possible contacts are probably

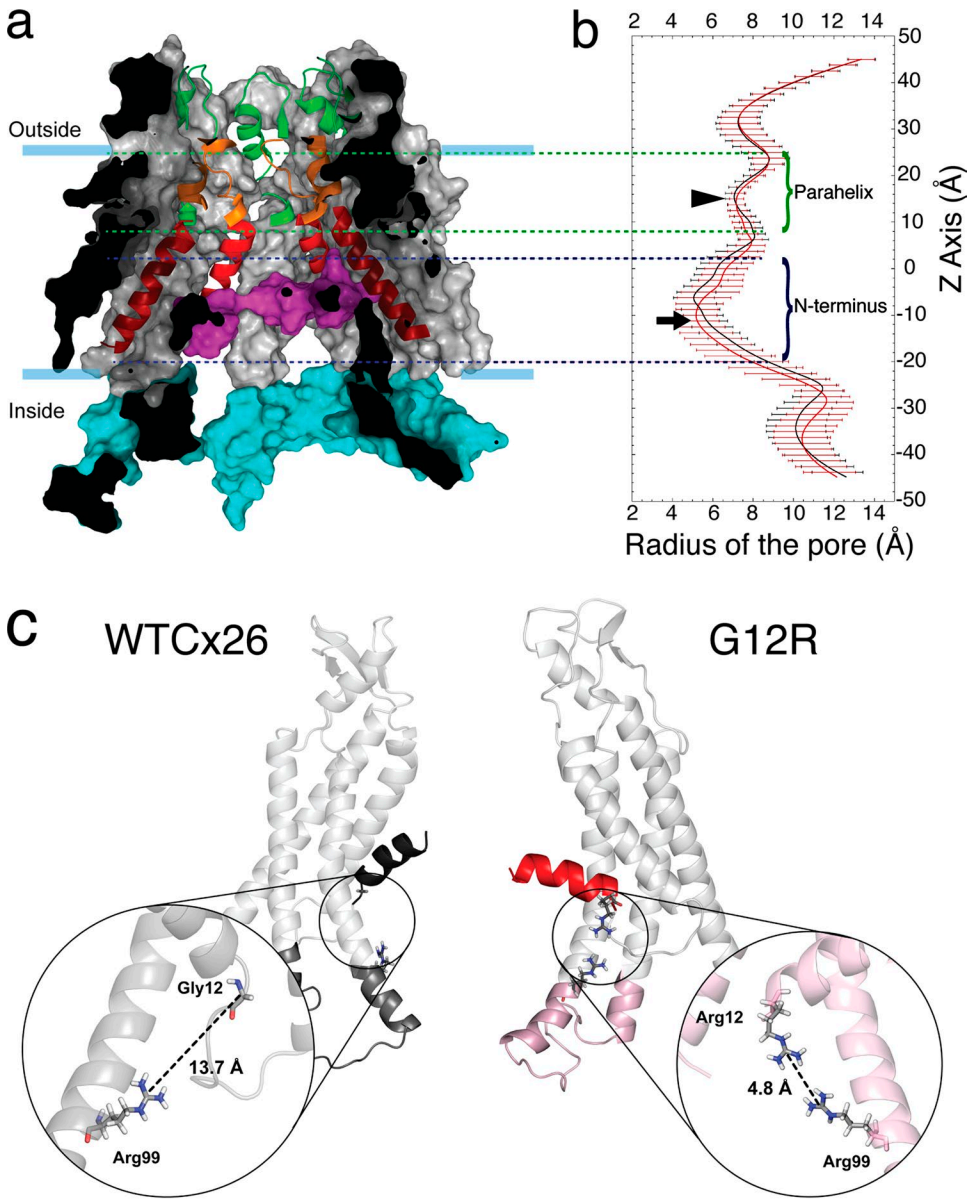

Figure 6. **G12R mutation causes the N terminus to move toward the cytoplasm and interact with residues in the intracellular loop. (a)** Structure of the WTCx26 hemichannel showing the N terminus (pink), TM1 (red), parahelix (orange), ELs (green), and intracellular loop (light blue). **(b)** Graph depicting the mean pore radius variation in function of pore axis during simulation. The region around the N terminus in G12R hemichannels is slightly displaced toward the cytoplasm. The narrowing of the pore in the parahelix regions does not change in G12R versus WTCx26. Data points represent mean ± SEM; *n* = 12. **(c)** Superimposition of representative monomers of WTCx26 (black) and G12R (red). Insets show the distances between residue 12 and the R99 in both WTCx26 (13.7 Å) and G12R (4.8 Å).

mediated by van der Waals interactions because no hydrogen bonds or salt bridges were observed. These contacts were absent in WTCx26, could represent a source for the stabilization of the displaced N terminus, and can be related to the change in the open probability of G12R hemichannels observed in single-hemichannel recordings.

Disrupting the interaction between R12 and R99 rescued the fast gating activation and reduced the open probability

Based on the in silico data, we hypothesized the R12–R99 interaction in G12R hemichannels "trapped" the N terminus in a position that impeded the conformational changes required for effective fast gating, leading to an increase in the open probability. To test this possibility, we replaced R99 on G12R by D (to strengthen the interaction), K (a conservative mutation), or A (to weaken the interaction) and determined the hemichannel properties of these mutants. Examples of macroscopic currents (Fig. 7, left) and single-hemichannel recordings obtained from excised inside-out or gap-free patches held at 40 mV (Fig. 7, right) show effective activation of the fast gate in WTCx26 revealed as a transition to the subconductance state (Fig. 7 a, O*r*) that is impaired in G12R hemichannels (Fig. 7 b). No hemichannel currents were detected in oocytes expressing G12R/R99D, but small conductance from endogenous channels can be

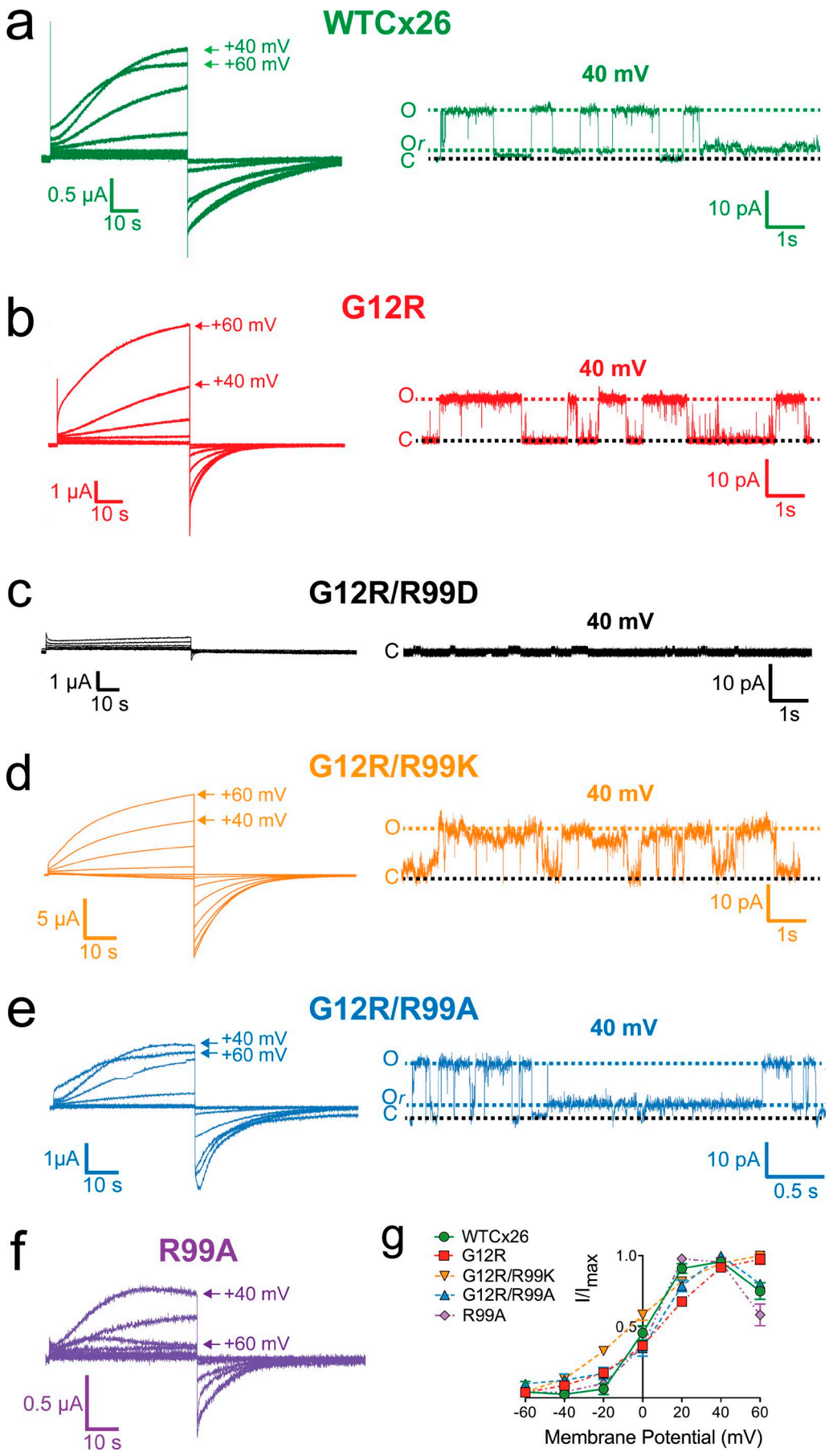
a
WTCx26
+40 mV
+60 mV
0.5 μA
10 s
40 mV
O
Or
C
10 pA
1s
b
G12R
+60 mV
+40 mV
1 μA
10 s
40 mV
O
C
10 pA
1s
c
G12R/R99D
1 μA
10 s
40 mV
C
10 pA
1s
d
G12R/R99K
+60 mV
+40 mV
5 μA
10 s
40 mV
O
C
10 pA
1s
e
G12R/R99A
+40 mV
+60 mV
1μA
10 s
40 mV
O
Or
C
10 pA
0.5 s
f
R99A
+40 mV
+60 mV
0.5 μA
10 s
g
WTCx26
G12R
G12R/R99K
G12R/R99A
R99A
I/Imax
1.0
0.5
-60
-40
-20
0
20
40
60
Membrane Potential (mV)

Table 1. **Summary of the number of contacts between residue 12 from each monomer and the extended intracellular loop region (residues 90–140), indicating the mean number of contacts for all simulations**

Monomer	WT	G12R
M1	0	<1 (7)
M2	0	12 (53)
M3	<1 (14)	3 (28)
M4	0	7 (35)
M5	0	2 (12)
M6	0	2 (22)

appreciated at the single-channel level (Fig. 7 c). In contrast, a conservative mutation in R99, R99K (G12R/R99K), produces macroscopic and single-hemichannel currents that resemble those of G12R (Fig. 7, d and g). G12R with R99 replaced by A (G12R/R99A) generated macroscopic hemichannel currents that decrease at the end of the test pulse at voltages ≥40 mV, similar to WTCx26 hemichannels (Fig. 7, e and g). At the single-channel level, G12R/R99A hemichannels exhibit short-lived transitions to the fully open state from the open substate and return to the subconductance state, where these hemichannels stay for several seconds as in WTCx26 (Figs. 7 e and S5). As a control, we also substituted R99 with A in WTCx26 (R99A) to evaluate whether this substitution alters the fast gate activation. This mutant generated functional macroscopic hemichannel currents that exhibit effective, fast gating. Interestingly, the traces obtained at 60 mV showed a marked decrease in macroscopic current amplitude compared with those observed in WTCx26 (Fig. 7, f and g). Thus, the biophysical behavior of G12R/R99A hemichannels resembles that of WTCx26 hemichannels and strongly indicates that R12–R99 interactions are responsible for the lack of fast gating activation in G12R.

Discussion

In connexin proteins, the N terminus is critical for structural and functional properties because it participates in oligomerization, channel closure, and voltage dependence (Verselis et al., 1994; Lagree et al., 2003; Kyle et al., 2008; Bargiello et al., 2012). Accordingly, we observed that the G12R mutation evoked hemichannel currents that did not reach a maximum and then a decrease at depolarizing voltages ≥40 mV, indicating that the fast gating mechanism is inoperative. An altered fast gating mechanism promoted by the G12R mutation was further confirmed by single-hemichannel recording experiments showing that the G12R hemichannels very seldom enter the subconductance state (Fig. 5). In addition, the G12R hemichannel closure is faster in response to hyperpolarizing voltage pulses, and the deactivation time constant becomes insensitive to $[Ca^{2+}]_o$, suggesting that the slow gate is also critically affected by this mutation.

The augmented current amplitude, together with a deactivation time constant that was almost independent of $[Ca^{2+}]_o$ concentrations, indicates that the G12R mutation modifies the slow gating kinetics (Pfahnl and Dahl, 1999). Ca^{2+} binds to residues located at the parahelix region (Zonta et al., 2014; Bennett et al., 2016; Lopez et al., 2016; Nielsen et al., 2017) to modulate the slow gate and stabilize the closed state of hemichannels (Trexler et al., 1996; Verselis and Srinivas, 2008; Lopez et al., 2013, 2016). Nevertheless, the mechanism of $[Ca^{2+}]_o$ action to stabilize the closing of hemichannels is controversial because it was recently proposed that the binding of Ca^{2+} does not cause conformational changes but instead creates an electrostatic "seal" that hinders the flux of ions through the pore (Bennett et al., 2016). This study contrasts with a previous one based on atomic force microscopy showing that, upon Ca^{2+} binding, hemichannels undergo large structural rearrangements that substantially reduce the pore size (Müller et al., 2002). Recently, a mechanism of gating by Ca^{2+} in connexin hemichannels has been reported. In this work, Lopez et al. (2016) demonstrate that the negatively charged residues D50 and E47 are essential for the stabilization of the closed state induced by Ca^{2+} binding to the Cx26 hemichannel. Our findings, that the K_d for Ca^{2+} in G12R hemichannels remained similar to that of WTCx26 (Fig. 3 c) and that both the pore diameter and the conformation of the parahelix were not affected in the mutant, suggest that the conformation of the putative Ca^{2+} binding site was not altered by the introduction of this charged residue. Likewise, the reduction of the deactivation time constant induced by this mutation strongly suggests that G12R did not uncouple Ca^{2+} binding from hemichannel closing.

The single-hemichannel conductance was not affected by the G12R mutation, in agreement with our molecular dynamic simulation results showing no radii differences along the pore between WT and mutant Cx26 hemichannels (Fig. 6 b). Reduction in single-channel conductance, impaired regulation by external Ca^{2+}, and augmented permeability to Ca^{2+} have been reported for KID mutations D50N, A40V, and G45E, respectively (Sánchez et al., 2013), suggesting that the underlying mechanism induced by KID mutations differs between mutations. In addition, our results strongly indicate that the N terminus is an active component of both the slow and fast gating mechanisms, and that both gates are coupled, which contrasts with previous studies on KID-associated mutations that affected only the slow gating mechanism, including mutation N14K that is also located in the N terminus of Cx26 (Sánchez et al., 2010, 2013, 2016). The involvement of the N terminus in the slow gating mechanism was also suggested by Rubinos et al. (2012). In this work, the authors showed that the antimalarial drug

Figure 7. **Disrupting the interaction between R12 and R99 rescues the fast gating activation.** Membrane currents recorded from oocytes under two-electrode voltage clamp in response to depolarizing voltage steps from a holding potential of −80 mV, stepped in 20-mV increments from −60 to 60 mV, and returned to −80 mV or representative patch-clamp single-channel recordings in oocytes from a holding potential of 0 mV and stepped to 40 mV. **(a–f)** Representative traces of macroscopic currents (left) and single-hemichannel recordings (right) from oocytes expressing WTCx26 (a), G12R (b), G12R/R99D (c), G12R/R99K (d), G12R/R99A (e), and R99A (f). Dashed lines in right panel indicate different current levels (O, fully open; Or, subconductance; C, closed). **(g)** Graph depicting the macroscopic current–voltage relationship of hemichannels calculated from the instantaneous tail currents. Data points represent mean ± SEM; $n = 3$.

Table 2. **Summary of the percentage of the total simulation time showing formation of hydrogen bonds between T86 and I82**

Monomer and replicas	M1	M2	M3	M4	M5	M6	Mean	SD
WTCx26								
R1	4	99	0	98	0	0	33.50	50.37
R2	26	98	0	40	17	0	30.17	36.03
R3	23	98	45	78	0	0	40.67	40.79
R4	6	99	0	93	0	12	34.83	47.62
Mean	14.50	98.50	11.25	77.25	4.25	3.00	34.79	41.39
SD	11.62	0.58	22.50	26.25	8.50	6.00		
G12R								
R1	89	89	6	97	39	0	50.33	44.14
R2	62	96	45	99	0	1	50.50	43.78
R3	80	78	52	97	0	4	51.83	41.21
R4	70	97	1	99	0	1	44.67	49.28
Mean	75.25	90.00	26.00	98.00	9.75	1.50	50.08	41.82
SD	11.76	8.76	26.22	1.15	19.50	1.73		

N-benzylquininium inhibits Cx50 hemichannels when added either extracellularly or intracellularly. *N*-benzylquininium promotes a drastic reduction of the open probability of hemichannels and the stabilization of the closed state, likely by binding specifically to the N terminus of Cx50 (Rubinos et al., 2012). Our results further show that intrinsic modifications of the N terminus (G12R mutation) modified the fast and slow gating of the hemichannel.

Molecular dynamics simulations indicate that the mechanism leading to altered biophysical properties of G12R hemichannels involves conformational changes in the N terminus. These conformational changes displaced the N terminus through the cytoplasm and allowed new contacts with residues located in the TM2/intracellular loop, reducing the N terminus flexibility (Fig. S3). Previous studies have shown the importance of G12 for the bending of the N terminus into the pore (Oshima et al., 2007; Maeda et al., 2009). Recent findings using ^{1}H-NMR on peptides mimicking the N terminus amino acidic composition of WTCx26 and G12R suggest that G12R does not affect the bending but makes the N terminus more flexible and less structured than that of WTCx26 (Batir et al., 2016). Although this study is in apparent disagreement with our finding that the N terminus exhibits reduced mobility (Fig. S3), the structure of the N terminus in solution can differ considerably from the structure of the same peptide surrounded by other protein segments. Moreover, our experimental results support our hypothesis that the absence of the fast gating activation in G12R hemichannels relies on restricted movement of the N terminus favored by the N terminus/intracellular loop attachment through R12–R99 interaction. Arginine–arginine interactions are common at the interface of oligomeric proteins, supporting protein stabilization (Magalhaes et al., 1994; Neves et al., 2012). The repulsion between the positive charges could be counteracted through induced dipole interactions, quaternary interactions among a cluster of arginines, neighboring negatively charged ions, hydrogen bonding residues, or mediating water molecules (Neves et al., 2012). In our simulations, we did not observe hydrogen bonding or water molecules mediating this possible interaction, but it has been proposed that an induced dipole could explain the ubiquitous arginine–arginine contact (Neves et al., 2012).

Impaired fast gating caused by conformational changes has been reported previously by Ri et al. (1999), in which altering the bend angle of the TM2 at the proline-kink site promotes a subtle change in the conductance value for the subconductance state in Cx32 gap junction channels. These authors hypothesized that the change in the conductance is a consequence of a narrowing of the cytoplasmic entrance at the N terminus via the straightening of a TM2 bend angle, thereby impairing the fast gating (Ri et al., 1999). We tested whether G12R leads to alterations in the bending of the proline-kink by analyzing the bend angles of the TM2 during our simulations. No differences were found in the proline-kink between WTCx26 and G12R hemichannels (Fig. S2 and Table 2), nor was a pore narrowing at the cytoplasmic entry observed (Fig. 6, a and b).

Recently, Sánchez et al. (2016) reported that the syndromic mutation N14K, localized at the N terminus, stabilized the open configuration of hemichannels by impairing the loop gating. The authors propose that a cation–π interaction between N14K and His100 impairs the slow gating without affecting the fast gating mechanism. This finding contrasts with our results showing that G12R virtually eliminates the fast gating. It is surprising that despite the proximity of N14K and G12R at the N terminus, the basis for the gain-of-function phenotype caused by these two mutations appears to differ significantly. Although neither N14 nor G12 is part of the α-helix, G12 is next to the last amino acid of the α-helix (G11). Thus, it is expected that a change from N14 to K would not greatly modify the structure of the N terminus, whereas a change from G12 to R should eliminate the α-helical bending. Moreover, it is possible that the G12R change favors a stronger and stable interaction

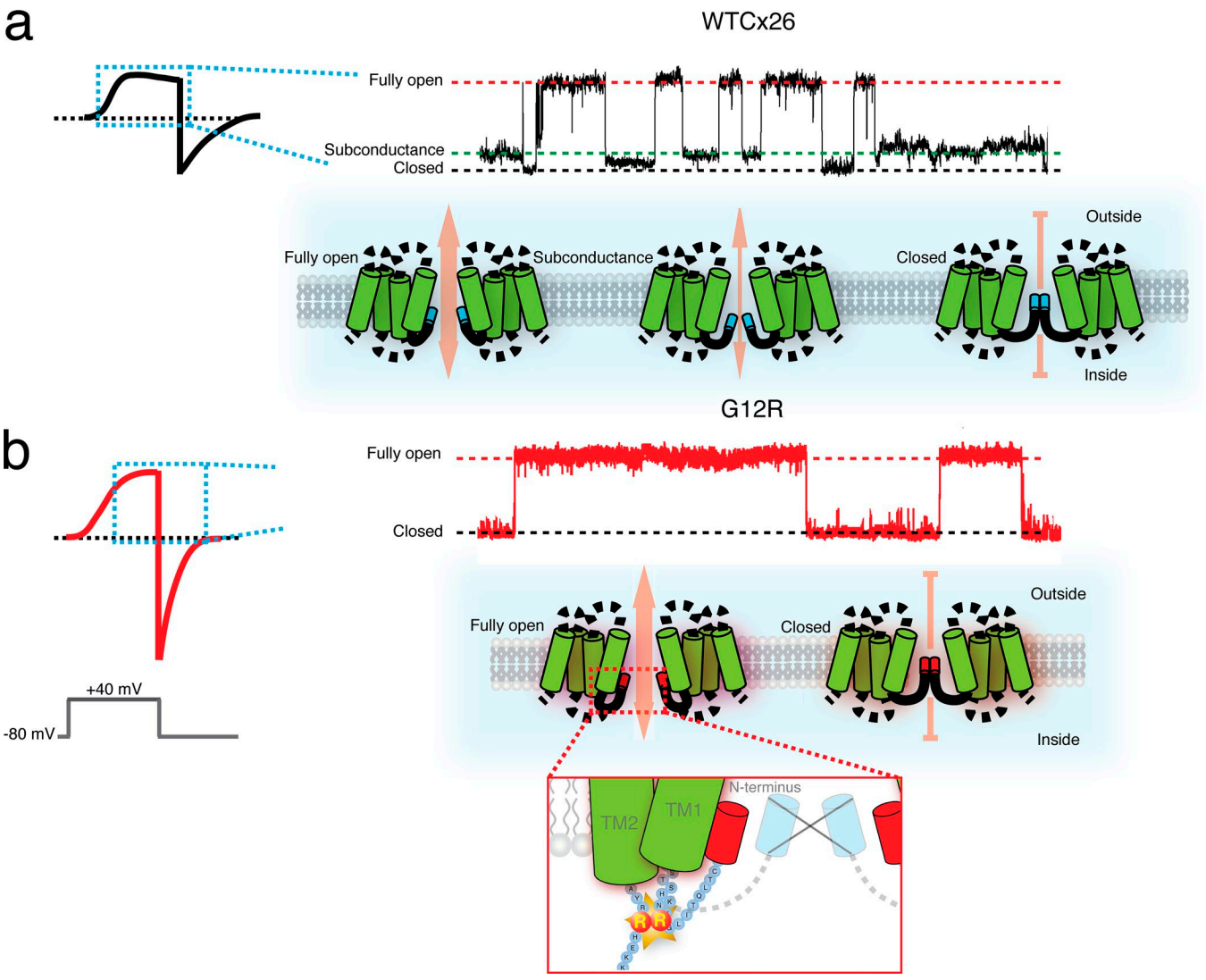

Figure 8. **Molecular model of the gain of function caused by G12R hemichannels. (a)** Cartoon depicting a macroscopic trace of WTCx26 hemichannel showing the reduction of current amplitude at 40 mV. At the single-channel level, this reduction in the current amplitude could be explained by the transition from the fully open state (red dashed line) to a subconductance state (green dashed line). **(b)** Cartoon depicting a macroscopic trace of G12R hemichannels illustrating the lack of current reduction observed in WTCx26. At the single-channel level, this difference could be caused by the lack of fast gating activation resulting from the absence of transitions to the subconductance state. This altered functioning would be caused by interactions between R12 and R99, which trap the N terminus in a rigid position, preventing its regular function and the activation of the fast gate.

between the N terminus and the intracellular loop than the ones produced by the N14K mutant, explaining why an N14K substitution would still allow the movement of the N terminus during the fast gating process.

The possibility of a functional interaction between the N terminus and the intracellular loop is also suggested by the recently reported cryo-electron microscopy structure of Inx-6 that reveals a structural association between these segments (Oshima et al., 2016). Notwithstanding that connexins and innexins have poor sequence homology, it is quite remarkable that both Inx6 and Cx26 have similar quaternary structures (Oshima et al., 2016). Thus, the suggested functional interaction between the N terminus and the intracellular loop in connexin cannot be excluded. Likewise, we note that replacing R99 with A in WTCx26 produced functional hemichannels with a fully functional fast gate (Fig. 7, f and g). However, the large decrease in current we observed in the case of this mutant when applying voltages >40 mV is probably caused by a fast gate with speedier kinetics and a long-lived subconductance state compared with the WTCx26 hemichannels; i.e., regarding the fast gate, the R99A mutant is a gain-of-function mutant.

In summary, we elucidated the molecular determinants underlying the gain of hemichannel function in the syndromic mutant, G12R. The basis for its increased function is the larger open probability rather than differences in single-channel conductance. These changes alter the position and the bending angle of the N terminus α-helix because of the rigidity that the substitution of G by R confers to this segment (Fig. 8 b). Based on our molecular modeling and the experimental results, we propose that the interaction between R12 and R99 traps the N terminus in a rigid position, preventing the N terminus from performing its function as blocking gating particle (Fig. 8 b, inset).

Acknowledgments

We thank Dr. José Ignacio García-Palacios and Dr. Viviana Berthoud for helpful discussions on the manuscript. We thank Claudia Pareja-Barrueto for helpful discussions on molecular dynamic simulations. We thank the National Laboratory of High Performance Computing–Chile center for providing computing time for molecular dynamic simulations, Powered@NLHPC.

This work was supported by Programa de Atracción e Inserción de Capital Humano Avanzado a la Academia (PAI 79170081) to I.E. García, Fondo Nacional de Desarrollo Científico y Tecnológico (3150634 to I.E. García, 1171240 to A.D. Martínez, 3140590 to G.F. Contreras, 1180434 to C. González, 1160574 to T. Pérez-Acle, and 1150273 to R. Latorre), Beca Comisión Nacional de Investigación Científica y Tecnológica–Program Formación de Capital Humano Avanzado/Doctorado Nacional/2017 to B.I. Pinto, Programa de Financiamiento Basal PFB16 Fundación Ciencia para la Vida, and the National Institutes of Health (RO1-GM099490 to J.E. Contreras). This work was partially supported by the Air Force Office of Scientific Research under award number FA9550-16-1-0384 to R. Latorre. The Centro Interdisciplinario de Neurociencia de Valparaiso is a Millennium Institute supported by the Millennium Scientific Initiative of the Chilean Ministry of Economy, Development, and Tourism (P029-022-F).

The authors declare no competing financial interests.

Author contributions: I.E. García, R. Latorre, A.D. Martínez, and C. González conceived this work. I.E. García, F. Villanelo, O. Alvarez, R. Latorre, and A.D. Martínez cowrote and coedited the final version of the manuscript. I.E. García, O. Alvarez, and R. Latorre designed the experimental strategies. I.E. García performed all the electrophysiological experiments. I.E. García, F. Villanelo, A. Pupo, and T. Pérez-Acle performed molecular dynamic simulations. All authors contributed to data analysis.

Merritt C. Maduke served as editor.

Submitted: 6 March 2017
Revised: 13 November 2017
Accepted: 21 March 2018

References

Arita, K., M. Akiyama, T. Aizawa, Y. Umetsu, I. Segawa, M. Goto, D. Sawamura, M. Demura, K. Kawano, and H. Shimizu. 2006. A novel N14Y mutation in Connexin26 in keratitis-ichthyosis-deafness syndrome: Analyses of altered gap junctional communication and molecular structure of N terminus of mutated Connexin26. *Am. J. Pathol.* 169:416–423. https://doi.org/10.2353/ajpath.2006.051242

Arora, A., P.J. Minogue, X. Liu, P.K. Addison, I. Russel-Eggitt, A.R. Webster, D.M. Hunt, L. Ebihara, E.C. Beyer, V.M. Berthoud, and A.T. Moore. 2008. A novel connexin50 mutation associated with congenital nuclear pulverulent cataracts. *J. Med. Genet.* 45:155–160. https://doi.org/10.1136/jmg.2007.051029

Bargiello, T.A., Q. Tang, S. Oh, and T. Kwon. 2012. Voltage-dependent conformational changes in connexin channels. *Biochim. Biophys. Acta.* 1818:1807–1822. https://doi.org/10.1016/j.bbamem.2011.09.019

Batir, Y., T.A. Bargiello, and T.L. Dowd. 2016. Structural studies of N-terminal mutants of connexin 26 and connexin 32 using 1H NMR spectroscopy. *Arch. Biochem. Biophys.* 608:8–19.

Bennett, B.C., M.D. Purdy, K.A. Baker, C. Acharya, W.E. McIntire, R.C. Stevens, Q. Zhang, A.L. Harris, R. Abagyan, and M. Yeager. 2016. An electrostatic mechanism for Ca(2+)-mediated regulation of gap junction channels. *Nat. Commun.* 7:8770. https://doi.org/10.1038/ncomms9770

Bergoffen, J., S.S. Scherer, S. Wang, M.O. Scott, L.J. Bone, D.L. Paul, K. Chen, M.W. Lensch, P.F. Chance, and K.H. Fischbeck. 1993. Connexin mutations in X-linked Charcot-Marie-Tooth disease. *Science.* 262:2039–2042. https://doi.org/10.1126/science.8266101

Bevans, C.G., and A.L. Harris. 1999. Regulation of connexin channels by pH. Direct action of the protonated form of taurine and other aminosulfonates. *J. Biol. Chem.* 274:3711–3719. https://doi.org/10.1074/jbc.274.6.3711

Dobrowolski, R., and K. Willecke. 2009. Connexin-caused genetic diseases and corresponding mouse models. *Antioxid. Redox Signal.* 11:283–295. https://doi.org/10.1089/ars.2008.2128

Ebihara, L. 1996. Xenopus connexin38 forms hemi-gap-junctional channels in the nonjunctional plasma membrane of Xenopus oocytes. *Biophys. J.* 71:742–748. https://doi.org/10.1016/S0006-3495(96)79273-1

Gaietta, G., T.J. Deerinck, S.R. Adams, J. Bouwer, O. Tour, D.W. Laird, G.E. Sosinsky, R.Y. Tsien, and M.H. Ellisman. 2002. Multicolor and electron microscopic imaging of connexin trafficking. *Science.* 296:503–507. https://doi.org/10.1126/science.1068793

García, I.E., J. Maripillán, O. Jara, R. Ceriani, A. Palacios-Muñoz, J. Ramachandran, P. Olivero, T. Perez-Acle, C. González, J.C. Sáez, et al. 2015. Keratitis-ichthyosis-deafness syndrome-associated Cx26 mutants produce nonfunctional gap junctions but hyperactive hemichannels when co-expressed with wild type Cx43. *J. Invest. Dermatol.* 135:1338–1347. https://doi.org/10.1038/jid.2015.20

García, I.E., F. Bosen, P. Mujica, A. Pupo, C. Flores-Munoz, O. Jara, C. González, K. Willecke, and A.D. Martínez. 2016. From hyperactive Connexin26 hemichannels to impairments in epidermal calcium gradient and permeability barrier in the keratitis-ichthyosis-deafness syndrome. *J. Invest. Dermatol.* 136:574–583.

Gerido, D.A., A.M. DeRosa, G. Richard, and T.W. White. 2007. Aberrant hemichannel properties of Cx26 mutations causing skin disease and deafness. *Am. J. Physiol. Cell Physiol.* 293:C337–C345. https://doi.org/10.1152/ajpcell.00626.2006

Goodenough, D.A., J.A. Goliger, and D.L. Paul. 1996. Connexins, connexons, and intercellular communication. *Annu. Rev. Biochem.* 65:475–502. https://doi.org/10.1146/annurev.bi.65.070196.002355

Kelsell, D.P., J. Dunlop, H.P. Stevens, N.J. Lench, J.N. Liang, G. Parry, R.F. Mueller, and I.M. Leigh. 1997. Connexin 26 mutations in hereditary non-syndromic sensorineural deafness. *Nature.* 387:80–83. https://doi.org/10.1038/387080a0

Kelsell, D.P., A.L. Wilgoss, G. Richard, H.P. Stevens, C.S. Munro, and I.M. Leigh. 2000. Connexin mutations associated with palmoplantar keratoderma and profound deafness in a single family. *Eur. J. Hum. Genet.* 8:141–144. https://doi.org/10.1038/sj.ejhg.5200407

Kwon, T., A.L. Harris, A. Rossi, and T.A. Bargiello. 2011. Molecular dynamics simulations of the Cx26 hemichannel: Evaluation of structural models with Brownian dynamics. *J. Gen. Physiol.* 138:475–493. https://doi.org/10.1085/jgp.201110679

Kyle, J.W., P.J. Minogue, B.C. Thomas, D.A. Domowicz, V.M. Berthoud, D.A. Hanck, and E.C. Beyer. 2008. An intact connexin N-terminus is required for function but not gap junction formation. *J. Cell Sci.* 121:2744–2750. https://doi.org/10.1242/jcs.032482

Lagree, V., K. Brunschwig, P. Lopez, N.B. Gilula, G. Richard, and M.M. Falk. 2003. Specific amino-acid residues in the N-terminus and TM3 implicated in channel function and oligomerization compatibility of connexin43. *J. Cell Sci.* 116:3189–3201. https://doi.org/10.1242/jcs.00604

Lampe, P.D., and A.F. Lau. 2000. Regulation of gap junctions by phosphorylation of connexins. *Arch. Biochem. Biophys.* 384:205–215. https://doi.org/10.1006/abbi.2000.2131

Lee, J.R., A.M. Derosa, and T.W. White. 2009. Connexin mutations causing skin disease and deafness increase hemichannel activity and cell death when expressed in Xenopus oocytes. *J. Invest. Dermatol.* 129:870–878. https://doi.org/10.1038/jid.2008.335

Lomize, M.A., A.L. Lomize, I.D. Pogozheva, and H.I. Mosberg. 2006. OPM: Orientations of proteins in membranes database. *Bioinformatics.* 22:623–625. https://doi.org/10.1093/bioinformatics/btk023

Lopez, W., J. Gonzalez, Y. Liu, A.L. Harris, and J.E. Contreras. 2013. Insights on the mechanisms of Ca^{2+} regulation of connexin26 hemichannels revealed by human pathogenic mutations (D50N/Y). *J. Gen. Physiol.* 142:23–35. https://doi.org/10.1085/jgp.201210893

Lopez, W., J. Ramachandran, A. Alsamarah, Y. Luo, A.L. Harris, and J.E. Contreras. 2016. Mechanism of gating by calcium in connexin hemichannels. *Proc. Natl. Acad. Sci. USA.* 113:E7986–E7995. https://doi.org/10.1073/pnas.1609378113

Maeda, S., S. Nakagawa, M. Suga, E. Yamashita, A. Oshima, Y. Fujiyoshi, and T. Tsukihara. 2009. Structure of the connexin 26 gap junction

channel at 3.5 A resolution. *Nature.* 458:597–602. https://doi.org/10.1038/nature07869

Magalhaes, A., B. Maigret, J. Hoflack, J.N. Gomes, and H.A. Scheraga. 1994. Contribution of unusual arginine-arginine short-range interactions to stabilization and recognition in proteins. *J. Protein Chem.* 13:195–215. https://doi.org/10.1007/BF01891978

Martí-Renom, M.A., A.C. Stuart, A. Fiser, R. Sánchez, F. Melo, and A. Sali. 2000. Comparative protein structure modeling of genes and genomes. *Annu. Rev. Biophys. Biomol. Struct.* 29:291–325. https://doi.org/10.1146/annurev.biophys.29.1.291

Mazereeuw-Hautier, J., E. Bitoun, J. Chevrant-Breton, S.Y. Man, C. Bodemer, C. Prins, C. Antille, J.H. Saurat, D. Atherton, J.I. Harper, et al. 2007. Keratitis-ichthyosis-deafness syndrome: Disease expression and spectrum of connexin 26 (GJB2) mutations in 14 patients. *Br. J. Dermatol.* 156:1015–1019. https://doi.org/10.1111/j.1365-2133.2007.07806.x

Müller, D.J., G.M. Hand, A. Engel, and G.E. Sosinsky. 2002. Conformational changes in surface structures of isolated connexin 26 gap junctions. *EMBO J.* 21:3598–3607. https://doi.org/10.1093/emboj/cdf365

Neves, M.A., M. Yeager, and R. Abagyan. 2012. Unusual arginine formations in protein function and assembly: Rings, strings, and stacks. *J. Phys. Chem. B.* 116:7006–7013. https://doi.org/10.1021/jp3009699

Nielsen, B.S., J.S. Alstrom, B.J. Nicholson, M.S. Nielsen, and N. MacAulay. 2017. Permeant-specific gating of connexin 30 hemichannels. *J. Biol. Chem.* 292:19999–20009. https://doi.org/10.1074/jbc.M117.805986

Oh, S., and T.A. Bargiello. 2015. Voltage regulation of connexin channel conductance. *Yonsei Med. J.* 56:1–15. https://doi.org/10.3349/ymj.2015.56.1.1

Olsson, M.H., C.R. Søndergaard, M. Rostkowski, and J.H. Jensen. 2011. PROPKA3: Consistent treatment of internal and surface residues in empirical pKa predictions. *J. Chem. Theory Comput.* 7:525–537. https://doi.org/10.1021/ct100578z

Oshima, A., K. Tani, Y. Hiroaki, Y. Fujiyoshi, and G.E. Sosinsky. 2007. Three-dimensional structure of a human connexin26 gap junction channel reveals a plug in the vestibule. *Proc. Natl. Acad. Sci. USA.* 104:10034–10039. https://doi.org/10.1073/pnas.0703704104

Oshima, A., K. Tani, and Y. Fujiyoshi. 2016. Atomic structure of the innexin-6 gap junction channel determined by cryo-EM. *Nat. Commun.* 7:13681. https://doi.org/10.1038/ncomms13681

Pfahnl, A., and G. Dahl. 1999. Gating of cx46 gap junction hemichannels by calcium and voltage. *Pflugers Arch.* 437:345–353. https://doi.org/10.1007/s004240050788

Pinto, B.I., I.E. García, A. Pupo, M.A. Retamal, A.D. Martínez, R. Latorre, and C. González. 2016. Charged residues at the first transmembrane region contribute to the voltage dependence of the slow gate of connexins. *J. Biol. Chem.* 291:15740–15752. https://doi.org/10.1074/jbc.M115.709402

Postic, G., Y. Ghouzam, and J.C. Gelly. 2015. An empirical energy function for structural assessment of protein transmembrane domains. *Biochimie.* 115:155–161. https://doi.org/10.1016/j.biochi.2015.05.018

Ri, Y., J.A. Ballesteros, C.K. Abrams, S. Oh, V.K. Verselis, H. Weinstein, and T.A. Bargiello. 1999. The role of a conserved proline residue in mediating conformational changes associated with voltage gating of Cx32 gap junctions. *Biophys. J.* 76:2887–2898. https://doi.org/10.1016/S0006-3495(99)77444-8

Richard, G., L.E. Smith, R.A. Bailey, P. Itin, D. Hohl, E.H. Epstein Jr., J.J. DiGiovanna, J.G. Compton, and S.J. Bale. 1998. Mutations in the human connexin gene GJB3 cause erythrokeratodermia variabilis. *Nat. Genet.* 20:366–369. https://doi.org/10.1038/3840

Rubinos, C., H.A. Sánchez, V.K. Verselis, and M. Srinivas. 2012. Mechanism of inhibition of connexin channels by the quinine derivative *N*-benzylquininium. *J. Gen. Physiol.* 139:69–82. https://doi.org/10.1085/jgp.201110678

Sánchez, H.A., G. Mese, M. Srinivas, T.W. White, and V.K. Verselis. 2010. Differentially altered Ca^{2+} regulation and Ca^{2+} permeability in Cx26 hemichannels formed by the A40V and G45E mutations that cause keratitis ichthyosis deafness syndrome. *J. Gen. Physiol.* 136:47–62. https://doi.org/10.1085/jgp.201010433

Sánchez, H.A., K. Villone, M. Srinivas, and V.K. Verselis. 2013. The D50N mutation and syndromic deafness: Altered Cx26 hemichannel properties caused by effects on the pore and intersubunit interactions. *J. Gen. Physiol.* 142:3–22. https://doi.org/10.1085/jgp.201310962

Sánchez, H.A., N. Slavi, M. Srinivas, and V.K. Verselis. 2016. Syndromic deafness mutations at Asn 14 differentially alter the open stability of Cx26 hemichannels. *J. Gen. Physiol.* 148:25–42. https://doi.org/10.1085/jgp.201611585

Segretain, D., and M.M. Falk. 2004. Regulation of connexin biosynthesis, assembly, gap junction formation, and removal. *Biochim. Biophys. Acta.* 1662:3–21. https://doi.org/10.1016/j.bbamem.2004.01.007

Söhl, G., and K. Willecke. 2003. An update on connexin genes and their nomenclature in mouse and man. *Cell Commun. Adhes.* 10:173–180. https://doi.org/10.1080/cac.10.4-6.173.180

Trexler, E.B., M.V. Bennett, T.A. Bargiello, and V.K. Verselis. 1996. Voltage gating and permeation in a gap junction hemichannel. *Proc. Natl. Acad. Sci. USA.* 93:5836–5841. https://doi.org/10.1073/pnas.93.12.5836

van Steensel, M.A., P.M. Steijlen, R.S. Bladergroen, E.H. Hoefsloot, C.M. van Ravenswaaij-Arts, and M. van Geel. 2004. A phenotype resembling the Clouston syndrome with deafness is associated with a novel missense GJB2 mutation. *J. Invest. Dermatol.* 123:291–293. https://doi.org/10.1111/j.0022-202X.2004.23204.x

Verselis, V.K., and M. Srinivas. 2008. Divalent cations regulate connexin hemichannels by modulating intrinsic voltage-dependent gating. *J. Gen. Physiol.* 132:315–327. https://doi.org/10.1085/jgp.200810029

Verselis, V.K., C.S. Ginter, and T.A. Bargiello. 1994. Opposite voltage gating polarities of two closely related connexins. *Nature.* 368:348–351. https://doi.org/10.1038/368348a0

Verselis, V.K., M.P. Trelles, C. Rubinos, T.A. Bargiello, and M. Srinivas. 2009. Loop gating of connexin hemichannels involves movement of pore-lining residues in the first extracellular loop domain. *J. Biol. Chem.* 284:4484–4493. https://doi.org/10.1074/jbc.M807430200

Woolf, T.B., and B. Roux. 1996. Structure, energetics, and dynamics of lipid-protein interactions: A molecular dynamics study of the gramicidin A channel in a DMPC bilayer. *Proteins.* 24:92–114. https://doi.org/10.1002/(SICI)1097-0134(199601)24:1%3C92::AID-PROT7%3E3.0.CO;2-Q

Yotsumoto, S., T. Hashiguchi, X. Chen, N. Ohtake, A. Tomitaka, H. Akamatsu, K. Matsunaga, S. Shiraishi, H. Miura, J. Adachi, and T. Kanzaki. 2003. Novel mutations in GJB2 encoding connexin-26 in Japanese patients with keratitis-ichthyosis-deafness syndrome. *Br. J. Dermatol.* 148:649–653. https://doi.org/10.1046/j.1365-2133.2003.05245.x

Zonta, F., F. Mammano, M. Torsello, N. Fortunati, L. Orian, and A. Polimeno. 2014. Role of gamma carboxylated Glu47 in connexin 26 hemichannel regulation by extracellular Ca^{2+}: Insight from a local quantum chemistry study. *Biochem. Biophys. Res. Commun.* 445:10–15. https://doi.org/10.1016/j.bbrc.2014.01.063